



Article

Spatial Pattern and Intensity Mapping of Coseismic Landslides Triggered by the 2022 Luding Earthquake in China

Zongji Yang ^{1,*} , Bo Pang ^{1,2}, Wufan Dong ^{1,2} and Dehua Li ^{1,2}¹ Institute of Mountain Hazards and Environment, Chinese Academy of Sciences, Chengdu 610041, China² University of Chinese Academy of Sciences, Beijing 100049, China

* Correspondence: yzj@imde.ac.cn; Tel.: +86-139-8214-4833

Abstract: On 5 September 2022, an Mw 6.6 earthquake occurred in Luding County in China, resulting in extensive surface rupture and casualties. Sufficient study on distribution characteristics and susceptibility regionalization of the earthquake-induced disasters (especially coseismic landslides) in the region has great significance to mitigation of seismic hazards. In this study, a complete coseismic landslide inventory, including 6233 landslides with 32.4 km² in area, was present through multi-temporal satellite images. We explored the distribution and controlling conditions of coseismic landslides induced by the 2022 Luding event from the perspective of epicentral distance. According to the maximum value of landslide area density, the geographical location with the strongest coseismic landslide activity intensity under the influence of seismic energy, the macro-epicenter, was determined, and we found a remarkable relationship with the landslide distribution and macro-epicentral distance, that is, both the landslide area and number density associatively decreased with the increase in macro-epicentral distance. Then, a fast and effective method for coseismic landslide intensity zoning based on the obvious attenuation relationship was proposed, which could provide theoretical reference for susceptibility mapping of coseismic landslides induced by earthquakes in mountainous areas. Additionally, to quantitatively assess the impact of topographic, seismogenic and lithological factors on the spatial pattern of coseismic landslides, the relationships between the occurrences of coseismic landslides and influencing factors, i.e., elevation, slope angle, local relief, aspect, distance to fault and lithology, were examined. This study provides a fresh perspective on intensity zoning of coseismic landslides and has important guiding significance for post-earthquake reconstruction and land use in the disaster area.

Keywords: coseismic landslides; Luding earthquake; spatial distribution; micro-epicenter; macro-epicenter



Citation: Yang, Z.; Pang, B.; Dong, W.; Li, D. Spatial Pattern and Intensity Mapping of Coseismic Landslides Triggered by the 2022 Luding Earthquake in China. *Remote Sens.* **2023**, *15*, 1323. <https://doi.org/10.3390/rs15051323>

Academic Editor: Rachid El Hamdouni

Received: 3 January 2023

Revised: 24 February 2023

Accepted: 24 February 2023

Published: 27 February 2023



Copyright: © 2023 by the authors. Licensee MDPI, Basel, Switzerland. This article is an open access article distributed under the terms and conditions of the Creative Commons Attribution (CC BY) license (<https://creativecommons.org/licenses/by/4.0/>).

1. Introduction

On 5 September 2022, at 12:52 p.m. local time, an Mw6.6 earthquake struck Luding, China [1]. The Luding event's epicenter is at 29.59°N, 102.08°E with a focus depth of 16 km. This earthquake damaged a vast amount of infrastructure, resulting in 88 deaths and over 400 injuries. Simultaneously, significant disasters such as coseismic landslides and collapses were induced, seriously endangering the personal security of local residents as well as reconstruction efforts.

Coseismic landslides are a geological disaster induced by earthquakes with strong destruction [2]. Thus, analyzing the distribution of coseismic landslides, investigating the correlations between coseismic landslides and triggering factors, and assessing the vulnerability of coseismic landslides are all crucial for guiding post-disaster reconstruction and secondary disaster prevention [3–5]. The landslide inventory serves as the foundation for analyzing and evaluating the mechanism of formation and spatial distribution of coseismic landslides, and many scholars have cataloged the coseismic landslide inventories for different earthquakes, such as the 1994 Mw6.7 Northridge event, America [6]; the

1999 Mw7.6 Chi-Chi event, China [7]; the 2008 Mw7.9 Wenchuan event, China [8] and the 2013 Mw6.6 Lushan event, China [9–11].

Coseismic landslide science research has become a focused issue, and numerous studies have been carried out on coseismic landslides of different earthquake magnitudes worldwide [12–20]. The findings indicate that the spatial pattern of coseismic landslides is attributed to the ground motion mode, vibration energy, geological environment and land type [21–25]. Without the restriction of geological environment, it is generally believed that the larger the earthquake energy level is, the more landslides there are with closer epicenter distance [26,27]. Keefer [28] discovered that the spatial frequency density of the coseismic landslides caused by the 1989 California earthquake decayed exponentially with the focal fault distance. Landslide susceptibility mapping and landslide sensitivity models considering different influencing factors are conducive to understanding landslide hazard risk [29]. Su et al. [30] found that the spatial distribution of the coseismic landslides induced by the 2008 Wenchuan event in Qingchuan County was mainly determined by lithology by using the logistic regression model. Zhao et al. [31] discovered that the majority of the coseismic landslides caused by the 2008 Wenchuan event and the 2013 Lushan event were concentrated in the Longmenshan fault's hanging wall, revealing the effect of tectonic mechanism on landslide distribution. All of these studies indicate that the controlling factors make great contributions to the occurrence and distribution of coseismic landslides. Thus, a thorough understanding of the interaction between coseismic landslides and controlling factors is critical for analyzing the formation mechanism of the distribution pattern [32].

Coseismic landslides are essentially the surface deformation caused by earthquakes [33], and their spatial distribution features are often associated with release of the seismic energy. However, there is no effective reference point that can indirectly reflect the release and spread of seismic energy on the surface. The epicenter of the earthquake can hardly reflect the location of the largest release of seismic energy, because some cases have shown that the coseismic landslide distribution is not strongly interrelated with the distance from the epicenter; for example, coseismic landslides induced by the Mw6.1 Ludian event in China were not concentrated at the epicenter but 5 km away [2], and many other earthquakes have similar deviations [18,24,32,34–36]. Consequently, it is very necessary to find a benchmark observation point that can reflect the intensity of the earthquake energy on the surface.

In this study, we focused on analyzing the spatial distribution pattern of coseismic landslides with elevation, slope angle, local relief, aspect, distance to fault and lithology. The maximum value of landslide area density (LAD) was utilized to determine the geographic location with the strongest landslide activity intensity affected by the Luding earthquake, which could be used as a key parameter to evaluate the impact of earthquake energy on the spatial pattern of coseismic landslides. Then, based on the landslide number density (LND) and landslide area density (LAD) with the grading threshold, the landslide intensity zoning was divided. The spatial pattern and formation mechanism of coseismic landslides were surveyed from the perspective of macro-epicentral distance. Our study gives detailed distribution characteristics of coseismic landslides induced by the 2022 Luding event which benefit ecological restoration and disaster management in the local region. Furthermore, we provide a novel reference for susceptibility zoning of coseismic landslides.

2. Materials and Methods

2.1. Study Area

The 2022 Luding event occurred in Luding County in China (Figure 1), at the south-eastern margin of the Tibetan Plateau. Affected by the Indian Ocean monsoon climate, the earthquake area is rainy in autumn and summer, providing sufficient hydrodynamic conditions for the occurrence of post-earthquake geological disasters. The bedrock adjacent to the river is constantly eroded for a long term, reducing the stiffness of the unloaded rock mass exposed to the air. In this case, the broken rock layers and weathered fracture on the valley slopes are conducive to the failure of the coseismic landslides. With regard to the

plate structure, the study region is situated at the intersection of the Indian Ocean plate and the Eurasian plate, which is the junction of the Longmenshan fault, the Xianshuihe fault and the Anninghe fault. The Indian Ocean plate continues to squeeze the Tibetan Plateau at a rate of 40–50 mm/a to the Eurasian plate every year, causing the crust in this area to move toward WE at a rate of 5–15 mm/a recorded by the global positioning system (GPS) [34]. The active crustal and tectonic movements in this area lay the groundwork for earthquake susceptibility, which is also the reason for the 2008 Wenchuan earthquake. The 2022 Luding event's epicenter, sited in the south of the Xianshuihe fault zone, is located in the Hailuogou scenic area of Moxi Town, only about 110 km away from the 2013 Ms7.0 Lushan earthquake [10]. The Xianshuihe fault, located in the famous Y-shaped fault region, is a sizable left-lateral strike-slip fault with considerable activity and NNW strike. It is about 400 km long and less than 300 km away from the Longmenshan fault in the north-east [37]. The 2022 Luding event is characteristic with a sinistral strike slip earthquake, and the seismogenic fault dips westward with a strike of 160° and an inclination of 80° . The maximum slip near the epicenter is about 184 cm, and the rupture duration is about 18 s. The earthquake gave rise to wide-ranging house damage and surface failure, affecting 82 townships of 12 counties. The intensity of the earthquake is elliptically distributed with the Xianshuihe fault as the long axis.

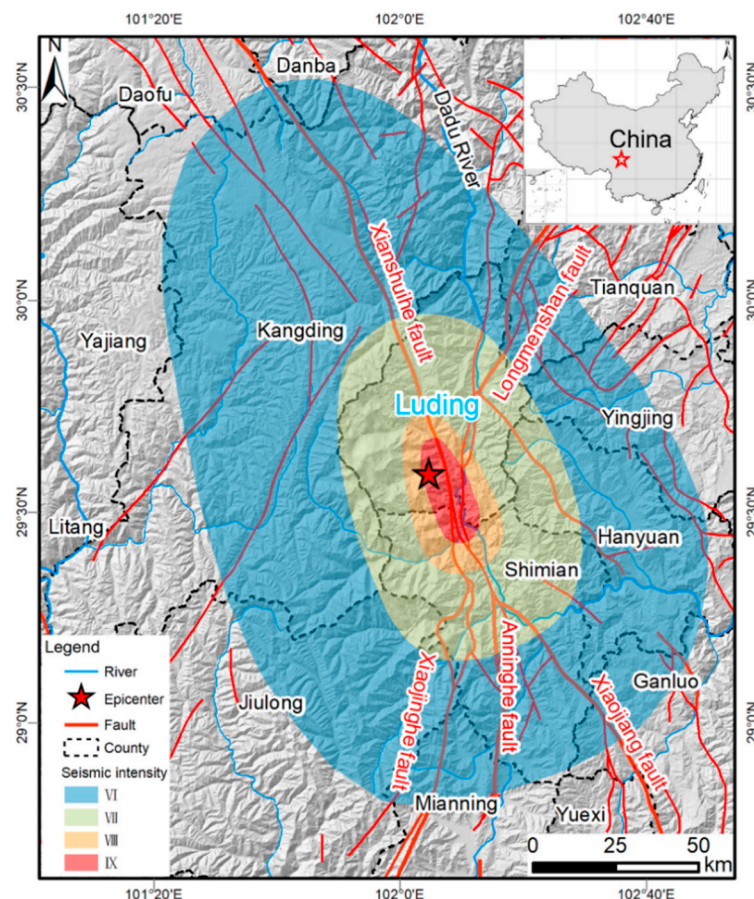


Figure 1. Location of the 2022 Luding earthquake in the southeastern Tibetan Plateau (the seismic intensity is from https://www.mem.gov.cn/xw/yjglbgzdt/202209/t20220911_422190.shtml; accessed on 15 September 2022).

2.2. Data and Methodology

It is not feasible to conduct a detailed on-site investigation for each coseismic landslide induced by the earthquake because of the rugged terrain in the region, so multi-temporal satellite images play a significant part in procuring coseismic landslide inventory

data [34,38,39]. To compile a comprehensive landslide inventory database, we conducted spot observations and satellite image interpretation. The post-earthquake satellite images included GF-2 (access time: 10 September 2022; resolution: 3.2 m), GF-6 (access time: 10 September 2022; resolution: 8 m) and Beijing-3 (access time: 10 September 2022; resolution: 3 m), covering an area of about $2 \times 10^4 \text{ km}^2$ (Figure 2). Coseismic landslides caused by the Luding event could be visually captured by comparing with pre-earthquake satellite images. The pre-earthquake satellite images included ZY-1 (access time: 8 July 2022; resolution: 2 m) and Sentinel-2 (access time: 29 April 2021; resolution: 10 m). We identified 6233 coseismic landslides according to the discrepancy in hue, texture, forest cover and other information of the satellite images (Figure 3). We outlined the profile of the coseismic landslide in ArcGIS platform to calculate the area of each coseismic landslide. Meanwhile, the field investigation gave great help for us to understand the coseismic landslide morphology more specifically.

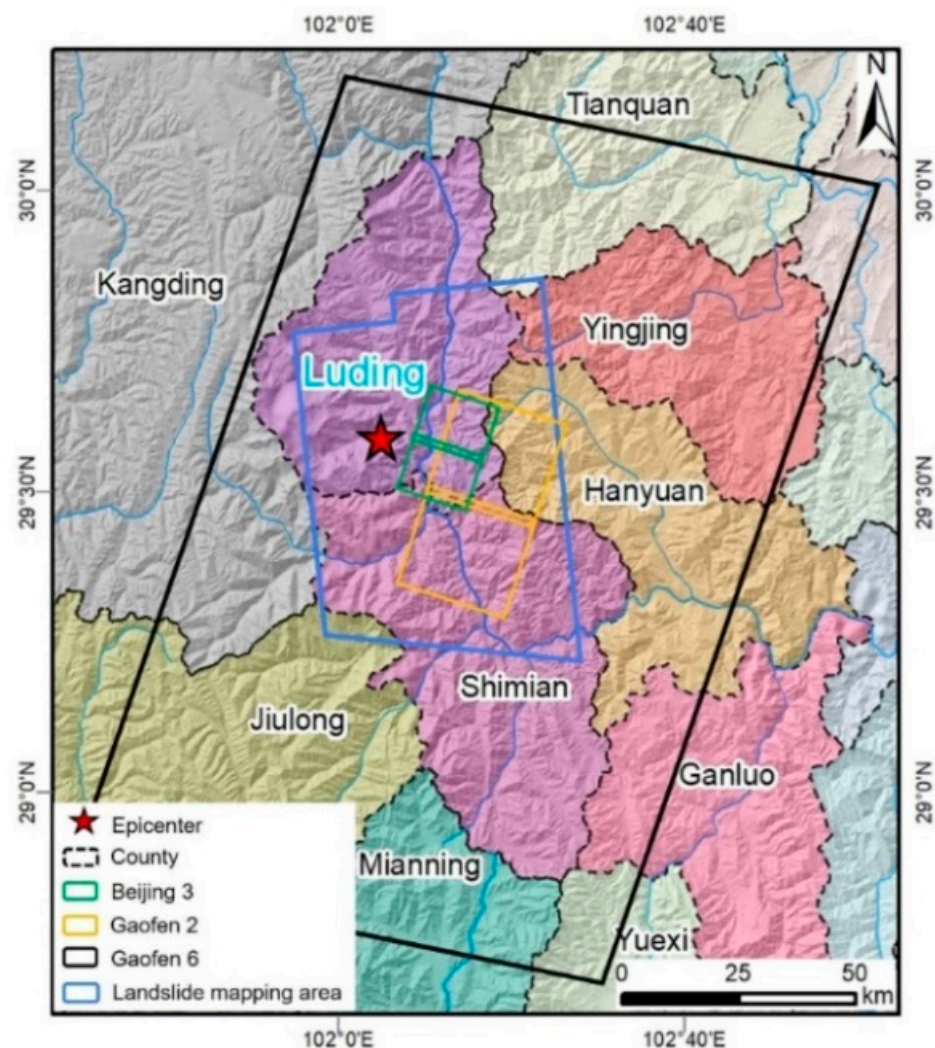


Figure 2. Coverage of satellite image.

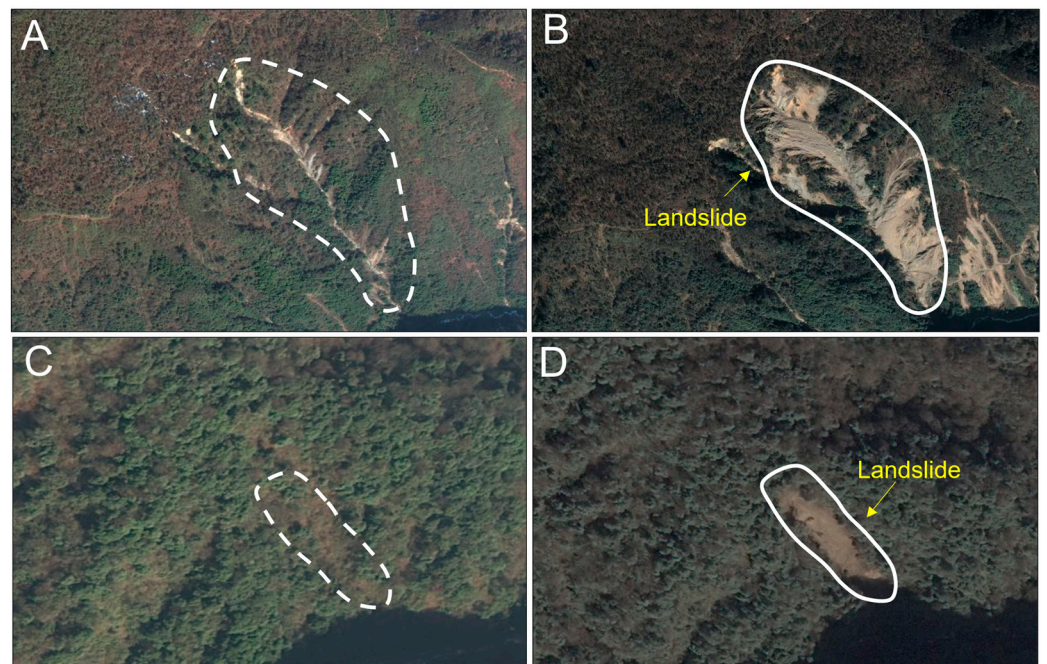


Figure 3. Coseismic landslides obtained from pre- (A,B) and post- (C,D) seismic satellite images.

In addition, to evaluate the impact of geology, seismic faults and topography on the spatial pattern of coseismic landslides, we collected elevation, slope angle, aspect, local relief, distance to seismogenic fault and lithology data. Slope angle, aspect and distance to seismogenic fault were collected from digital elevation model (DEM) data with 30 m resolution (<http://www.gscloud.cn/>; accessed on 15 September 2022). Geological data including lithology and faults were extracted from a geological map digitized to 1:250,000 scale. Subsequently, the spatial pattern of coseismic landslides with different factors was statistically analyzed in ArcGIS platform.

Landslide abundance is a commonly used indicator to measure the distribution scale of coseismic landslides [37,40]. We analyzed landslide area density (LAD) and landslide number density (LND) of the coseismic landslide inventory through the grid-based maps produced by small squares of 1 km in length and width with an area of 1 km² (LAD refers to the total area of coseismic landslides per km²; LND refers to the total number of coseismic landslides per km²).

3. Results

3.1. Landslide Inventory

The energy aroused by the Mw6.6 Luding event is dozens of times smaller than that of the 2008 Wenchuan event [41], so the type of landslide differs from that of the Wenchuan event dominated by a large landslide. The spot survey reveals that the type of coseismic landslide is mainly shallow landslide including natural slopes and cut slopes, manifested as mountain peeling. Affected by seismic amplification effect along the slope and shear vibration, coseismic landslides are mainly developed in the steep and gentle slope break section of watershed, ridge and mountainside, mainly including soil collapses, strongly weathered bedrocks (mainly granite in lithology) and rockfalls (Figure 4).



Figure 4. Typical coseismic landslide types induced by the Luding event. (A) collapse flow; (B–F) soil landslides.

The coseismic landslides triggered by the 2022 Luding event are primarily concentrated along the Moxi–Wanggongping section and distributed along both sides of the seismogenic fault. The coseismic landslides are most concentrated about 10 km to the south of Moxi Town, which is also a severe disaster area of coseismic landslides. However, there are relatively few coseismic landslides at the epicenter (Figure 5A,B). Landslide densities (LAD and LND) are mainly located south of the epicenter and are asymmetrically distributed along the fault. Over a 3545 km² affected region, the 2022 Luding event caused 6233 coseismic landslides at a minimum. In accordance with the correlations between the area affected by coseismic landslides and earthquake magnitude, most events are located at the lower side of the envelope (dashed and solid lines) [26,27]. The 2022 Luding earthquake follows the criteria as well (Figure 6A). For the landslide number and total area, the Luding event is as close to the trend line as the previous earthquakes and is located below the fitting line, demonstrating the coseismic landslides are more numerous and larger in area than the earthquakes with same magnitude (Figure 6B,C) [33,42]. With regard to the coseismic landslide frequency density p , Figure 6D compares the distribution frequency of the landslide area with other earthquakes near the fault: the 2008 Wenchuan event (Mw 7.9), the 2013 Lushan event (Mw 6.6) and the 2017 Jiuzhaigou event (Mw 6.5) [18]. The 2022 Luding earthquake also fits the inverse gamma distribution, i.e., $\log(p) = -1.56 \times \log(A) + 3.0$. For the size distribution, we divided the coseismic landslides into five scales in Table 1.

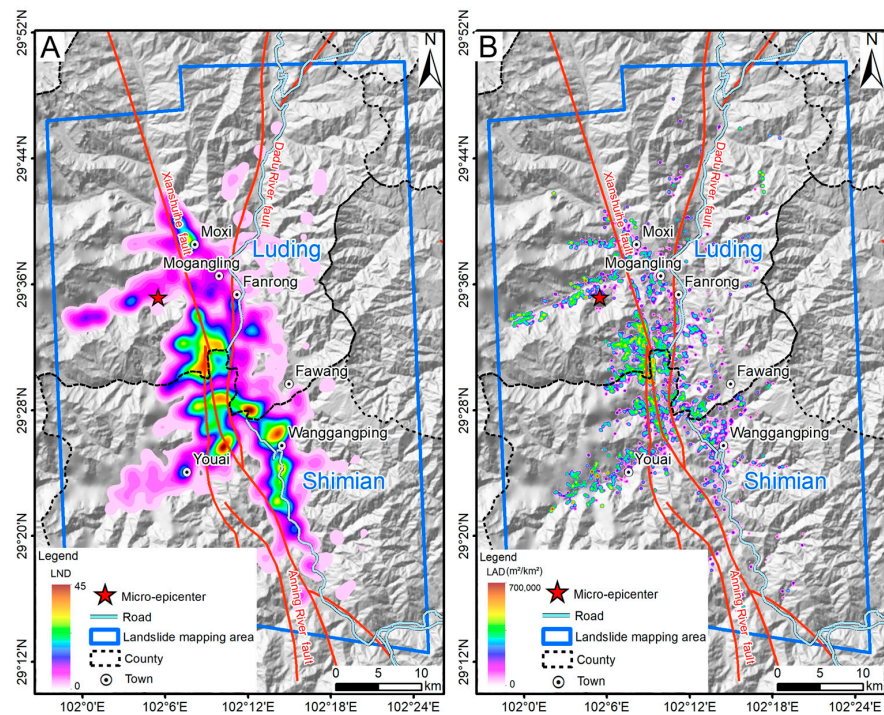


Figure 5. Regional distribution of the coseismic landslides caused by the 2022 Luding event. (A) LND; (B) LAD.

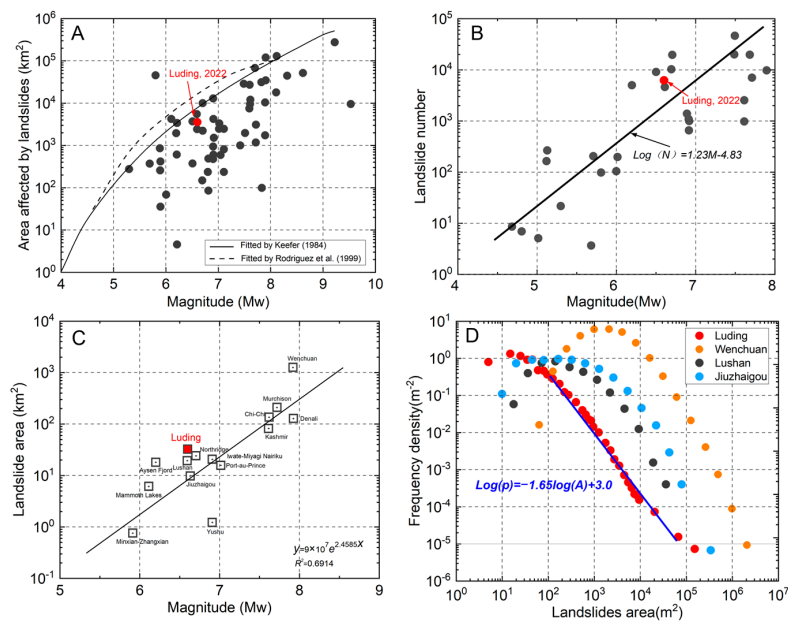


Figure 6. Comparison of landslide inventory caused by the 2022 Luding event with other events. (A) the earthquake magnitude and the area affected by coseismic landslides (the black circle represents other earthquake cases from [26,27]); (B) the earthquake magnitude and the number of landslides (other cases are referred from [33,42]); (C) the total area of landslides and earthquake magnitude; (D) the correlations of landslide area frequency density for the 2022 Luding event, the 2008 Wenchuan event, the 2013 Lushan event and the 2017 Jiuzhaigou event. The base map of (C,D) are referred from [18].

Table 1. Distribution characteristics of coseismic landslides in different scales.

Classification	Landslide Area/m ²	Landslide Number	Total Ratio %
I	areas < 1000	2337	37.50
II	1000 ≤ areas < 5000	2409	38.64
III	5000 ≤ areas < 10,000	720	11.56
IV	10,000 ≤ areas < 50,000	688	11.04
V	areas ≥ 50,000	79	1.26
Total		6233	100

3.2. Spatial Pattern of Coseismic Landslides with Epicentral Distance

The epicentral distance for a coseismic landslide is considered as the distance from the coseismic landslide point to the seismogenic epicenter [2,34]. The spatial distribution of coseismic landslides is significantly impacted by the epicentral distance as well [28,43]. However, the initial rupture site of the Xianshuihe fault which is regarded as the micro-epicenter of the 2022 Luding event is not the most intensive zone of the coseismic landslides (Figure 7A). The pertinence between the distribution of the coseismic landslide and the micro-epicentral distance is not correlative; the closer to the micro-epicenter of the earthquake, the lower occurrence probability of the coseismic landslides is, manifesting that the initial rupture point of the seismogenic fault cannot generate the energy that can trigger the occurrence of large-scale coseismic landslides. Since landslide concentration can assess earthquake damage to the ground [44], we set the geographical location at the maximum landslide area density as the macro-epicenter (located in 29.5°N, 102.15°E). Figure 7B clearly demonstrates that coseismic landslides are concentrated near the macro-epicenter, and the coseismic landslide number decreases inch by inch with the extension of the macro-epicentral distance. Notably, coseismic landslides with large area (red circle) appear sporadically far away from the macro-epicenter on the Xianshuihe fault's hanging wall, indicating that the spatial distribution of coseismic landslides caused by the 2022 Luding event is not only driven by the magnitude of seismic energy, but may be related to other influencing factors as well, such as terrain and stratum [43].

In order to quantitatively obtain the relationships between the spatial pattern of coseismic landslides and the epicentral distance, we compared the correlations between LAD and LND with the micro- and macro-epicenter, respectively, where the distance from the epicenter is the Euclidean distance [3]. The LAD and LND of coseismic landslides have no obvious correlation with micro-epicenter distance (Figure 8A,B), but are quantitatively related with macro-epicenter distance, i.e., $y = 216881 \times x^{(-0.69)}$ with $R^2 = 0.956$ for LAD and $y = 0.011x^2 - 0.89x + 18.78$ with $R^2 = 0.791$ for LND (Figure 8C,D). Therefore, the macro-epicentral distance, as a metric, can better indicate the degree of harm on the surface in the process of seismic energy diffusion when exploring the spatial pattern of coseismic landslides triggered by earthquakes compared with the micro-epicentral distance. Emphatically, the reason why two different functions were used is that we wanted to obtain a best goodness-of-fit of each LAD and LND with satisfying R^2 to ensure that the subsequent quantitative analysis had a smaller deviation.

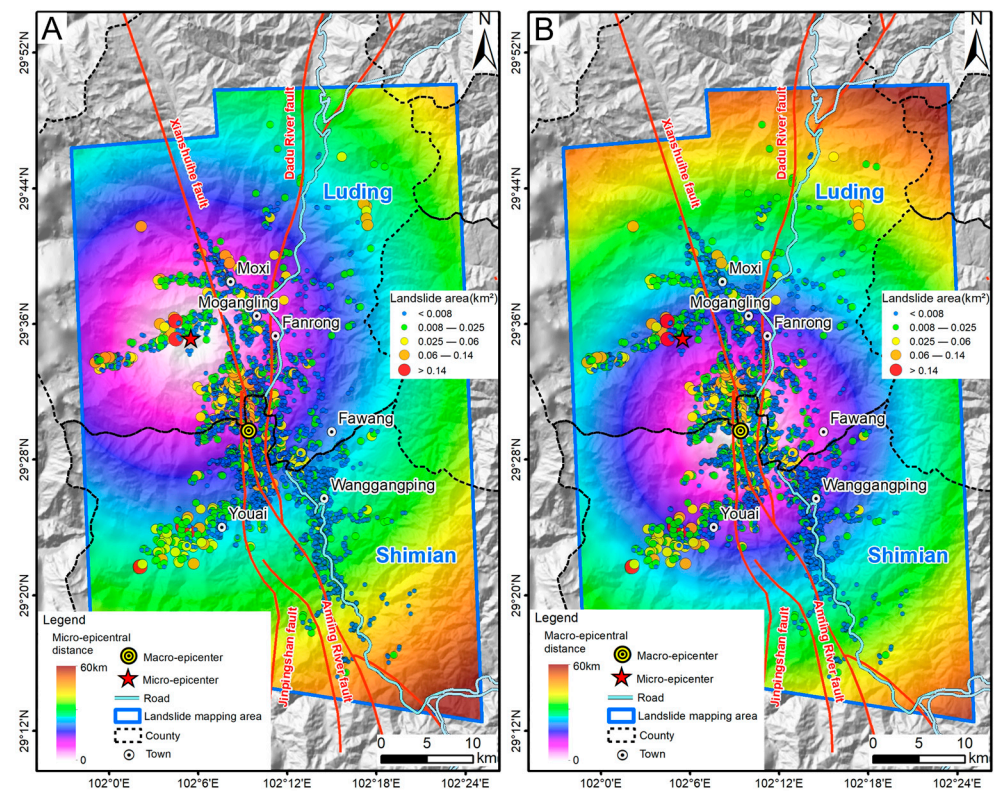


Figure 7. Coseismic landslide distribution with epicentral distance. (A) micro-epicenter; (B) macro-epicenter.

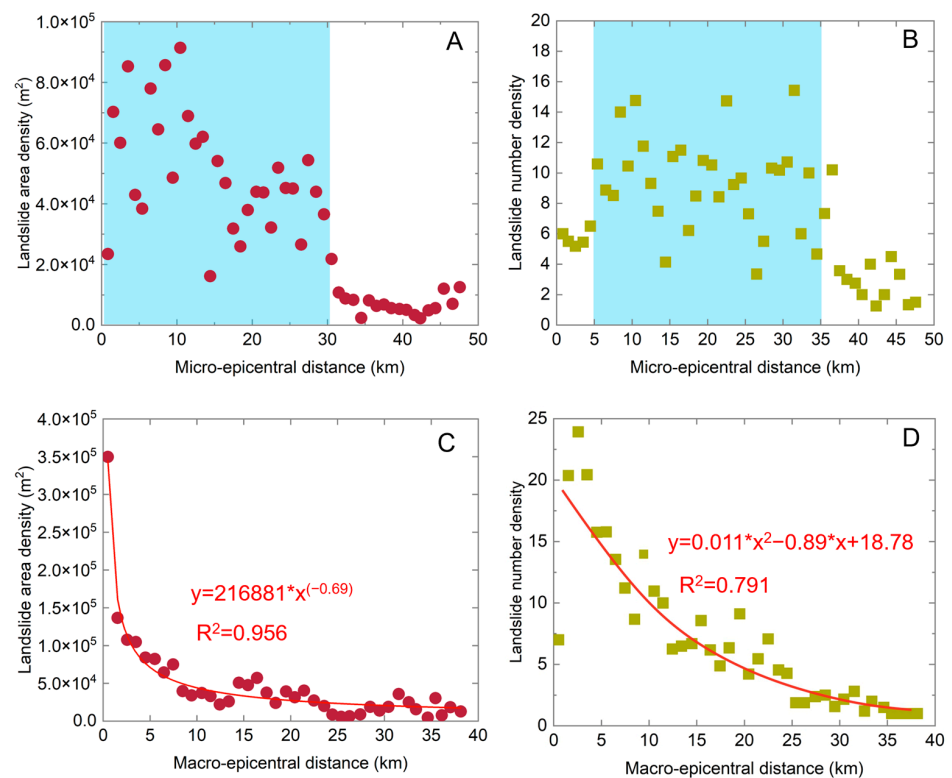


Figure 8. Correlations between epicentral distance and landslide abundance (LAD and LND). (A,B) micro-epicenter; (C,D) macro-epicenter.

The spatial distribution of coseismic landslides takes on a clear gradient reduction tendency with the macro-epicentral distance in Figure 8. Based on this, considering the

landslide abundance, we proposed a fast and effective landslide intensity zoning method. The partition thresholds were calculated by the fitting function of LAD and LND with macro-epicenter distance in Table 2. Figure 9 is the landslide intensity map, depicting the spatial pattern of coseismic landslides in high-, mid- and low-prone area. According to statistics, the landslide number induced by the 2022 Luding earthquake in the high-, mid- and low-prone areas is 3829, 2164 and 240, respectively, with areas for 18.78 km², 12.30 km² and 1.34 km², respectively.

Table 2. Zoning value for landslide intensity.

Intensity Level	LAD (m ² /km ²)	LND	Macro-Epicentral Distance (km)
high-prone	50,000	10	11.5
mid-prone	25,000	5	22.9
low-prone	18,000	1	39.0

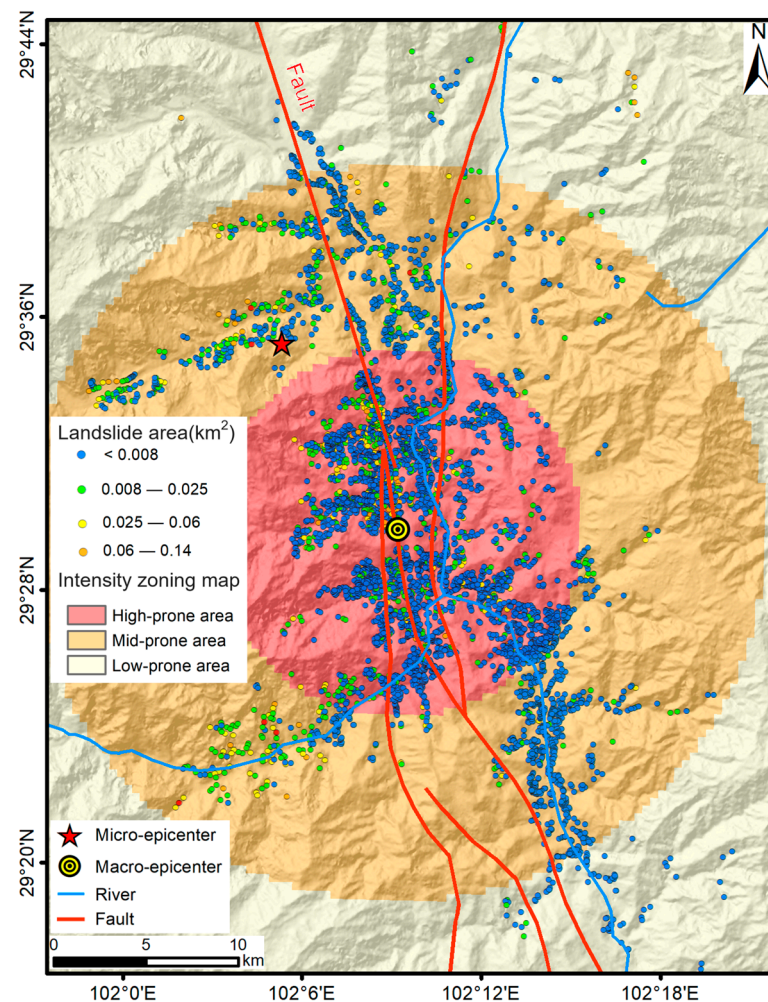


Figure 9. Landslide intensity map.

3.3. Controlling Factors of Coseismic Landslide Distribution

Earlier research has found the nonuniformity in the coseismic landslide spatial pattern [20,45]. In this part, we aim to analyze the related influencing factors that lead to the phenomenon. Six related factors were taken into account to thoroughly understand the impact of controlling factors on the spatial pattern of coseismic landslides.

3.3.1. Topographic Factors

Elevation is a crucial topographic feature that affects the occurrence of coseismic landslides [24]. The spatial pattern of coseismic landslides caused by the 2022 Luding event with elevation was statistically analyzed based on DEM data (Figure 10A). For the landslide abundance, the LAD and LND are mainly concentrated in the range of 0–10 km from the macro epicenter and 10–35 km from the micro epicenter, and the larger values of the LAD and LND correspond to the elevation of 1400–1800 m (Figure 10B,C). For the individual landslide, the regions with the elevation ranking from 1000 to 2300 m are more prevalent for coseismic landslides (Figure 10D), with 5518 in total, accounting for 88.5% of the total. This prone area is a concentrated area of human activities (housing construction, mining, road construction and water conservancy projects), manifesting that these activities have a significant effect on the susceptibility of coseismic landslides. After the elevation exceeds 1500 m, the landslide number decreases gradually as the elevation rises. With the increasing elevation, the landslide area expands inch by inch, and the relationship is approximately $\text{Log}(y) = 0.52x + 2.35$ (where y is landslide area, x is elevation of landslide).

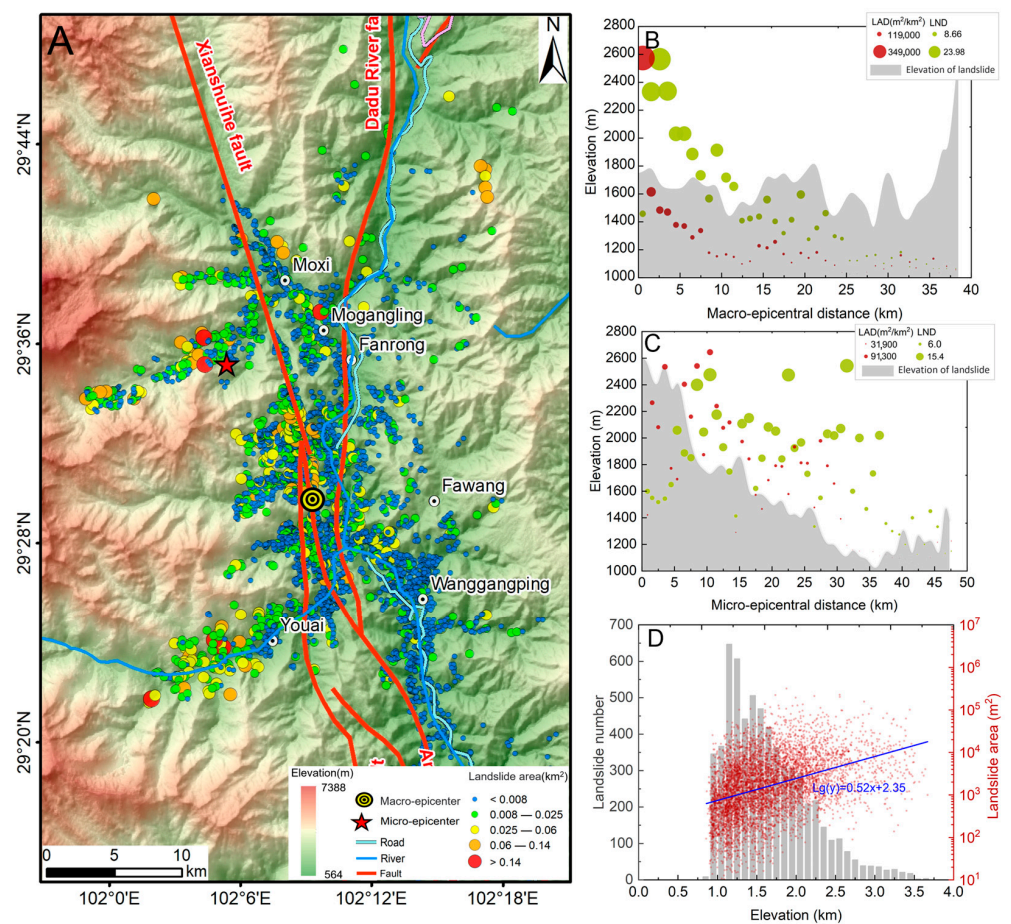


Figure 10. (A) coseismic landslide distribution with elevation; (B,C) elevation of landslide with macro- and micro-epicentral distance; (D) individual landslide distribution with elevation.

As is known, the slope angle has a massive effect on the distribution pattern of coseismic landslides. The shear stress of the rock mass along the slope increases with the increasing angle, in which case slope failure occurs in steep places even without earthquake. Numerous studies have found that most landslides are concentrated around 20–50° [8,46]. Figure 11A–C shows that the most intensive landslide abundance (LAD and LND) occurs in the range of 30–40°, and the epicentral distance has little influence on the angle. Throughout the whole affected region, most of the landslide cluster is in the range

of 30 to 40°, totaling 4211, accounting for 67.6% of the total (Figure 11D). The landslide number shows a Gaussian distribution with the slope angle, reaching a peak at 35°.

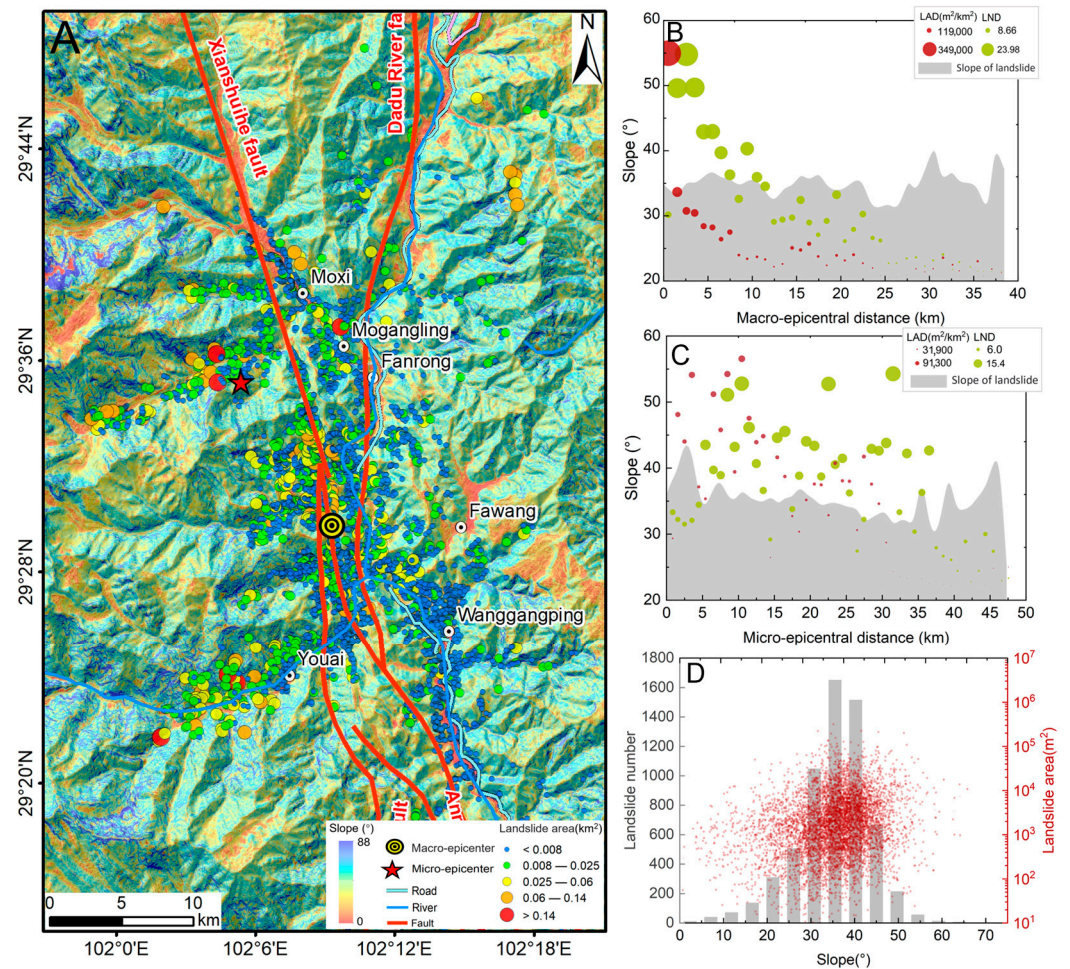


Figure 11. (A) coseismic landslide distribution with slope angle; (B,C) slope angle with macro- and micro-epicentral distance; (D) individual landslide distribution with slope angle.

Local relief reflects the surface distortion and is also a quantitative indicator of the gravity potential energy in the region. Figure 12A depicts the coseismic landslide distribution with the local relief as the background (the local relief map is extracted in GIS platform based on 5×5 km window). As shown in Figure 12B,C, the most intensive LAD and LND are primarily gathered at the elevation difference ranking from 1400 to 1800 m. In addition, 90.7% of the landslides occurred in the elevation of 1200–2000 m, 5654 in total (Figure 12D).

During seismic wave propagation, the development of coseismic landslides would be impacted by the aspect of slope [40,45,47]. In addition, the influence of climate on slopes with different aspect is also not consistent, resulting in different sensitivity to the instability of slopes of different aspect. For example, the slope on the windward side is more prone to runoff due to rain erosion, and these unstable slopes are more likely to be triggered by earthquakes [13]. The spatial pattern of landslides in various slope aspects is shown in Figure 13A. Statistical analysis indicates that the aspect distribution presents primarily S-E predominance, consistent with the Xianshuihe fault's strike and the travelling direction of seismic waves, which can be explained by the stronger amplification effect on the slopes that are back to the seismic wave's propagation direction (Figure 13B,C) [48]. The coseismic landslides in N, NE, E, SE, S, SW, W and NW are 292, 740, 1081, 1245, 908, 737, 684 and 546, respectively, accounting for 4.7%, 11.9%, 17.3%, 20.0%, 14.6%, 11.8%, 11.0% and 8.7% of total, respectively.

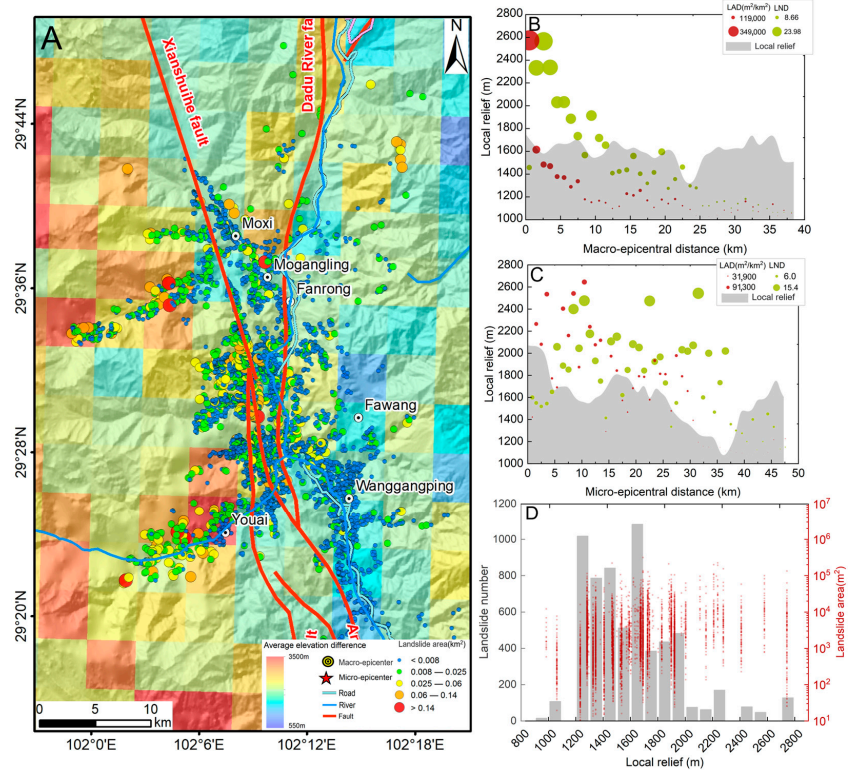


Figure 12. (A) coseismic landslide distribution with local relief; (B,C) local relief with macro- and micro-epicentral distance; (D) individual landslide distribution with local relief.

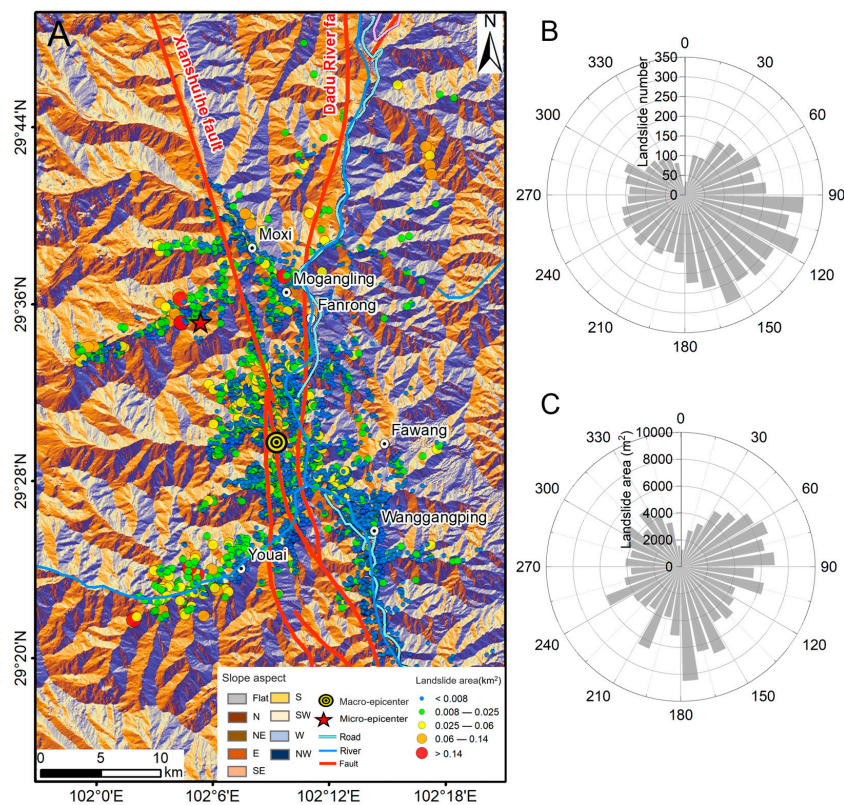


Figure 13. (A) coseismic landslide distribution with slope aspect; (B) landslide number and aspect; (C) landslide area and aspect.

3.3.2. Seismogenic Factor

The distribution of coseismic landslides is predominantly controlled by the seismogenic fault, confirmed in other cases [28,37]. In general, coseismic landslides occur on both sides of the seismogenic fault, and the landslide number exponentially decreases as the distance to fault increases [49]. Figure 14A shows the landslide distribution pattern with different distance to fault. The landslide distributed in 0–5 km, 5–10 km, >10 km counts 4652, 1242 and 339, respectively, occupy 74.7%, 19.9 and 5.4% of total, respectively, and follows an exponential distribution $y = 1613 \times e^{(-x/4.2)} - 17.5$ (Figure 14B). Furthermore, the area of the coseismic landslides increases with the increase in the distance to fault, following a relationship of approximately $\text{Log}(y) = 0.04x + 3.05$.

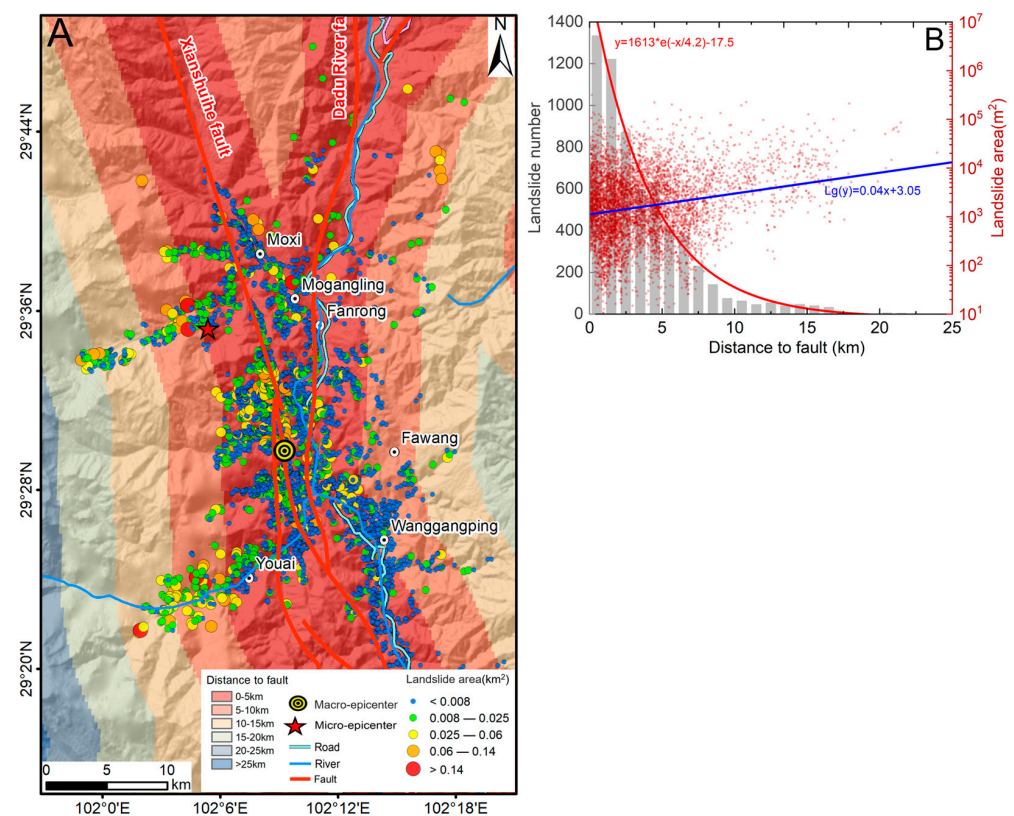


Figure 14. (A) coseismic landslide distribution with distance to fault; (B) correlations between landslide distribution and distance to fault.

3.3.3. Geological Factor

Figure 15A shows the landslide spatial distribution pattern related to different strata. The potential impact areas of landslides have complex controlling lithologies, mainly including sedimentary rocks and intrusive rocks. Statistically, there are 2261, 1358, 956, 745, 369, 227 and 177 landslides occurring in granite, quartz diorite, tuff sandstone, metasandstone, quartz sandstone, carbonatite and ultrabasic rock, accounting for 36.3%, 21.9%, 15.3%, 12.0%, 5.9% and 2.3% of the total, respectively (Figure 15B). Granite is the main factor affecting the distribution of coseismic landslides. This “weakening effect” may be that the granite rock mass has very developed fissure joints due to the long-term tectonic activity in this area, leading to the decline of rock mass stability [40,50].

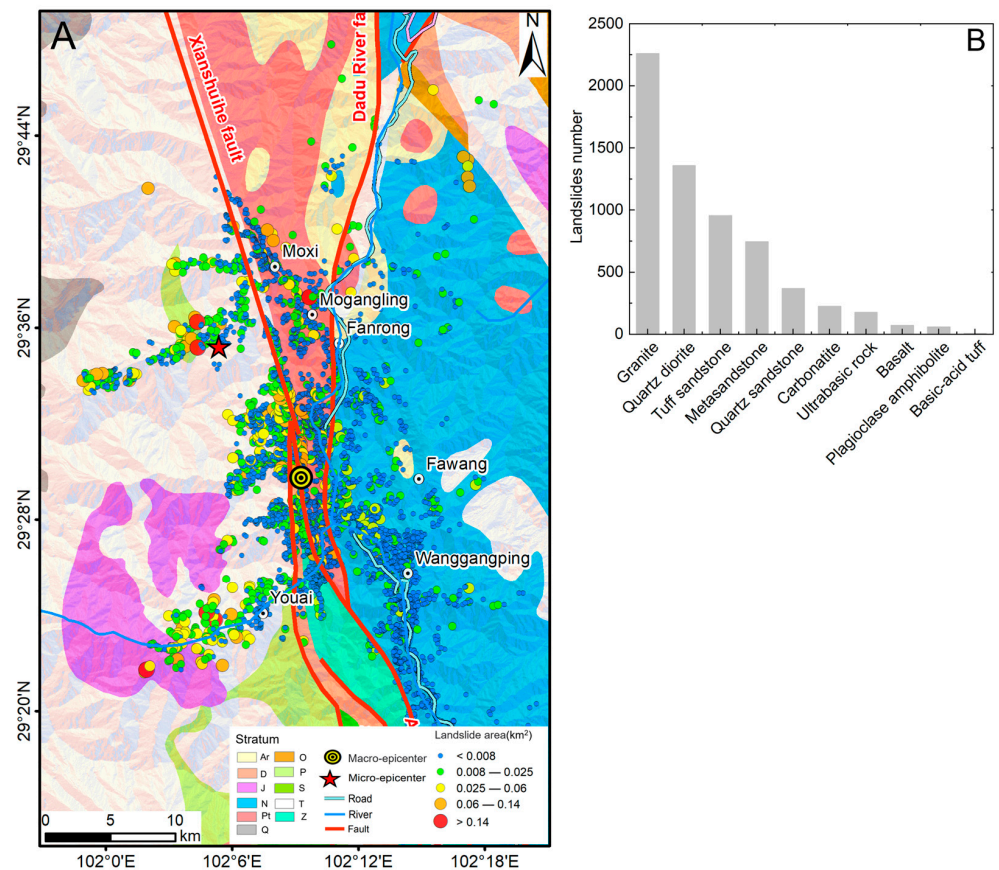


Figure 15. (A) coseismic landslide distribution with lithology; (B) correlations between landslide number and lithology.

4. Discussion

4.1. Landslide Intensity Mapping

Typically, seismic events cause varying extents of damage to the site. The Environmental Macroseismic Scale (EMS-98) can evaluate the level of ground damage of earthquakes, mainly determined by the damage to objects or buildings and the feelings of people in the epicentral area [51]. However, the EMS-98 is limited in a sparsely populated mountain area. Subsequently, the Environmental Seismic Intensity Scale (ESI-07) was exclusively developed to evaluate the impact of earthquakes in mountain areas on the natural environment [52]. The ESI-07 defines earthquake damage by considering the occurrence and area distribution of earthquake environmental effect (EEE), including surface fault, geological uplift and settlement, landslide, rockfall, liquefaction, surface subsidence and tsunami [53]. Gosar [54] determined the seismic intensity map of the 1998 Mw 5.6 Krn Mountains earthquake by investigating the spatial pattern of 78 rockfalls triggered by the earthquake, indicating that the seismic damage can be reflected by the spatial pattern of coseismic landslides/rockfalls when the geo-disasters caused by the seismic event are dominated by slope movements. The intensity isoseism can be determined by the distribution probability of landslides/rockfalls of different sizes. However, it is not easy to gauge the intensity isoseism and coseismic landslide regional intensity when there are mixed numerous coseismic landslides/rockfalls with various size. The 2022 Luding event also conforms to this characteristic.

The intensity zoning map of coseismic landslides developed in this paper reflected the concentration of coseismic landslides from the distribution abundance, which could therefore avoid some uncertainty caused by non-uniform landslide distribution with variable size using ESI-07. The threshold values of different partition levels are determined according to the specific distribution of coseismic landslides induced by earthquakes with

different magnitudes. Emphatically, the landslide intensity map may not accurately reflect the macro earthquake intensity, but provide a suggestion. The landslide intensity map is the manifestation of the joint control of topographic conditions, seismogenic faults and stratum lithology, which is helpful for people to better comprehend the damage caused by seismic events on the spatial scale. The intensity mapping of coseismic landslides is not only applicable to the 2022 Luding event, but is also worth exploring in other earthquakes in the future. The zoning method based on macro-epicentral distance has better guiding significance for post-earthquake landslide prevention, rapid evaluation of seismic intensity and land-use planning.

4.2. Tectonic Genesis for the Discrepancy of Landslide Distribution

Many earthquakes have occurred on the Xianshuihe fault in history due to abundant tectonic activities (Figure 16). According to the record, the GPS horizontal displacement velocity in the seismogenic fault's hanging wall is significantly larger than that in the footwall and the direction of velocity is nearly parallel, which contributes to a sinistral strike-slip earthquake for the 2022 Luding event. The spatial pattern of coseismic landslides is profoundly affected by the fault slip mode. Coseismic landslides caused by strike-slip earthquakes, particularly deep landslides, are often localized within 5 km of the seismogenic fault [55]. The coseismic landslide spatial pattern of the Luding event also conforms to this rule. The majority of coseismic landslides towards SE also reveal that there is a strong correlation between the direction of seismic waves and the distribution of coseismic landslides. Additionally, the preponderance of the coseismic landslides localized in the hanging wall implies that the Xianshuihe fault's hanging wall exhibits more robust vibrational characteristics than the footwall wall [1].

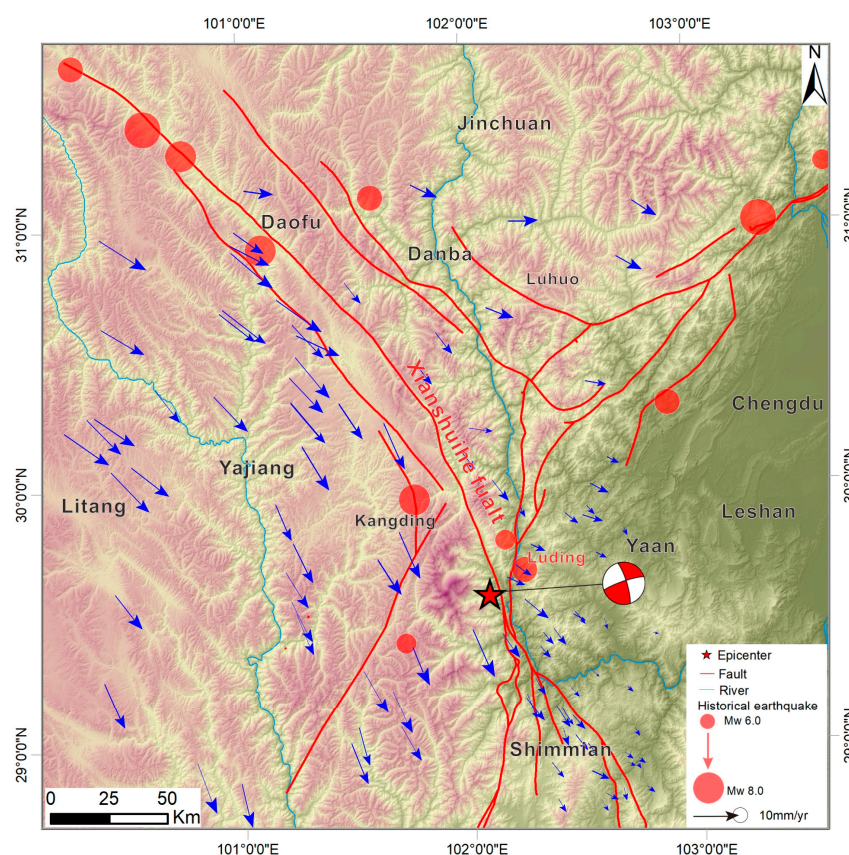


Figure 16. Regional map showing the velocity field of GNSS horizontal motion before the 2022 Luding M6.8 earthquake (from <http://data.earthquake.cn>; accessed on 20 October 2022) and the historical earthquakes (>Mw6) since 1900 (from USGS.gov | Science for a changing world; accessed on 20 October 2022).

The location of the micro-epicenter, projection point from source to surface, is determined by inversion from nearby stations based on seismic waves released by the initial rupture of the fault. Seen in Figure 17A, the distance between the fault and the micro-epicenter is a particular amount related to dip angle of the fault, slip angle and focal depth. The accumulated stress in the process of plate compression is released suddenly after an earthquake, and the fault plane releases seismic energy onto the surrounding area (Figure 17B). During energy transmission, the seismic energy attenuates along the path [56], resulting that the micro-epicenter is not the place with the largest surface energy, which explains why the coseismic landslide spatial pattern is more closely related to the macro-epicentral distance, and the macro-epicenter has more control over the occurrence and spatial pattern of coseismic landslides than the micro-epicenter. In fact, the specific position of the macro-epicenter depends vastly on the rupture direction of the seismogenic fault during an earthquake. On account of the southward rupture of the seismogenic fault during the Luding event [57], the macro-epicenter is located on the south side of the micro-epicenter. This phenomenon is also confirmed in the 2008 Wenchuan earthquake because the controlled area of coseismic landslides induced by the Wenchuan earthquake is just on the northward rupture of the seismogenic fault, rather than the micro-epicenter [24]. The impact of tectonics on spatial pattern of coseismic landslides induced by the 2022 Luding event is emphasized, which differs from the combination of topography and tectonics proposed by Zhao et al. [1]. Thus, we propose that more focus should be placed on the macro-epicentral distance rather than the micro-epicentral distance in the future study of the spatial characteristics of coseismic landslides controlled by epicentral distance.

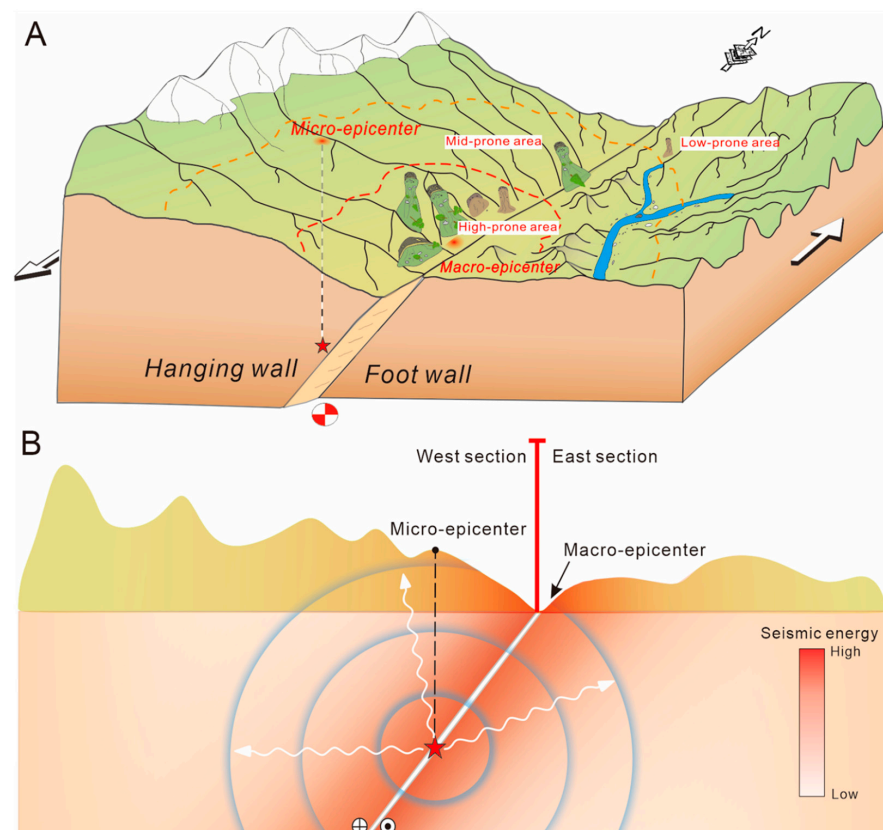


Figure 17. Schematic Diagram of the 2022 Luding Mw6.6 earthquake. (A) three-dimensional focal mechanism; (B) propagation process of earthquake energy.

4.3. Limitations

This study aims to compile a thorough coseismic landslide inventory for the 2022 Luding event and analyze the impact of potential controlling factors on the distribution

pattern of coseismic landslides. However, there are still a few drawbacks in landslide mapping and corresponding analysis.

For landslide mapping, we extracted 6233 landslides totaling 32.4 km² in size, covering the area 50 km away from the epicenter. However, some small landslides may not be effectively identified due to the inadequate resolution of satellite images and lush vegetation, resulting in a modest undercount of landslides compared to the actual situation. Despite the fact that the data for the landslide inventory is overestimated, the present data of coseismic landslides covered the whole meizoseismal region and will not change the assessment results.

In addition, the mismatch between the DEM data (resolution: 30 m × 30 m) and the geological map at 1:250,000 scale may lead to deviation in results, but this can be avoided because it is not our main research purpose. The weathering of granite can also be considered in the spatial pattern of coseismic landslides to obtain more comprehensive outcomes, which requires more detailed geological and lithological mapping at a scale larger than 1:250,000 (such as 1:25,000, 1:10,000 or 1:5000). These further studies are able to add to our awareness of the relationship between geology and coseismic landslides and additional details of granite weathering grade maps as a predisposing factor [58], which contributes to our comprehension of landslide distribution for further landslide risk and hazard assessment.

With regard to the analysis of epicentral distance, we took the place with the maximum value of LAD in the study region as the macro-epicenter of the earthquake. However, whether this location is the projection point on the surface where the maximum energy is released when the fault breaks remains to be debated. Surely, the macro-epicenter, the location where the surface is most affected by the earthquake, is related to the release of earthquake stress. Moreover, we solely explored the correlation between epicentral distance and spatial pattern of coseismic landslides from the macroscopic phenomenon on the surface, without considering the intrinsic influence of seismic physical parameters on landslides, such as seismic attenuation acceleration (α), ground motion period (T), seismic vibration duration (t), etc. because these not only involve the research content of the earthquake itself, but also involve the relationship between seismic physical parameters and landslide material characteristic parameters. If the seismic physical parameters and the coseismic landslide physical parameters are studied together, there will be many complex functional relationships, and no satisfactory solution can be obtained.

5. Conclusions

In order to clarify the spatial pattern characteristics of coseismic landslides caused by the 2022 Luding event, we provided a complete landslide inventory containing 6233 coseismic landslides through remote sensing interpretation and field investigation. The associations between the spatial pattern of coseismic landslides and six potential controlling factors encompassing elevation, slope angle, slope aspect, local relief, distance to the seismogenic fault and lithology were analyzed. We found that mostly coseismic landslides are primarily concentrated on the slopes at elevation from 1000 to 2300 m with slope of 30–40°, an E–S aspect and local relief from 1200 to 2000 m. The main coseismic landslide occurred in granite, accounting for the largest proportion (36.3%). Within 5 km from the fault, there is an intensive concentration of coseismic landslides, clustered along both sides of the fault. The seismogenic fault and focal mechanism play an important role in the spatial pattern of coseismic landslides in this earthquake.

Through the maximum value of LAD of coseismic landslides, the position of the macro-epicenter is established. The LAD and LND of coseismic landslides exhibit a fairly satisfactory function relationship with the macro-epicentral distance (compared with the micro epicenter) as follows: $y = 216,881 \times x^{(-0.69)}$ for LAD with $R^2 = 0.956$; $y = 0.011x^2 - 0.89x + 18.78$ for LND with $R^2 = 0.791$. Then, the intensity distribution map of coseismic landslides was proposed. The intensity distribution of landslides can reveal the dissipation process of seismic energy propagation and provide information on the

damage of the earthquake to mountain areas. In addition, we also revealed the reason why the spatial pattern of coseismic landslides deviated from the micro-epicenter in the 2022 Luding earthquake from the perspective of tectonic activities, assisting us in better comprehending the distribution mechanism of earthquake-induced landslides.

Author Contributions: Author Contributions: Conceptualization, Z.Y.; methodology, Z.Y.; software, B.P.; validation, B.P., W.D. and D.L.; formal analysis, B.P.; investigation, Z.Y.; resources, Z.Y.; data curation, B.P.; writing—original draft preparation, B.P.; writing—review and editing, B.P., W.D. and D.L.; visualization, B.P.; supervision, Z.Y.; project administration, Z.Y.; funding acquisition, Z.Y. All authors have read and agreed to the published version of the manuscript.

Funding: This work was financially supported by the Projects of Western Light in Chinese Academy of Sciences (Grant Nos. E1R2090) and the National Natural Science Foundation of China (Grant Nos. U22A20565).

Data Availability Statement: The datasets used and analyzed during the current study are available from the corresponding authors upon reasonable request.

Acknowledgments: The authors are grateful to the editors and the anonymous reviewers for their extensive and profound comments and suggestions, which substantially improved the quality of the paper. The authors are thankful for the data support from “China Earthquake Networks Center, National Earthquake Data Center. (<http://data.earthquake.cn>; accessed on 20 October 2022)”. We also thank Zhang Jianqiang, Hu Kaiheng, Chen Huayong, Zhao Bo, Zhu Lei, Zhang Weifeng, Liu Qiao and Zou Qiang for their support in collecting the data and interpretation.

Conflicts of Interest: The authors declare no conflict of interest.

References

1. Zhao, B.; Hu, K.-H.; Yang, Z.-J.; Liu, Q.; Zou, Q.; Chen, H.-Y.; Zhang, B.; Zhang, W.-F.; Zhu, L.; Su, L.-J. Geomorphic and tectonic controls of landslides induced by the 2022 Luding earthquake. *J. Mt. Sci.* **2022**, *19*, 3323–3345. [[CrossRef](#)]
2. Zou, Y.; Qi, S.W.; Guo, S.F.; Zheng, B.W.; Zhan, Z.F.; He, N.W.; Huang, X.L.; Hou, X.K.; Liu, H.Y. Factors controlling the spatial distribution of coseismic landslides triggered by the Mw 6.1 Ludian earthquake in China. *Eng. Geol.* **2022**, *296*, 106477. [[CrossRef](#)]
3. Karakas, G.; Nefeslioglu, H.A.; Kocaman, S.; Buyukdemircioglu, M.; Yurur, T.; Gokceoglu, C. Derivation of earthquake-induced landslide distribution using aerial photogrammetry: The January 24, 2020, Elazig (Turkey) earthquake. *Landslides* **2021**, *18*, 2193–2209. [[CrossRef](#)]
4. Miles, S.B.; Keefer, D.K. Evaluation of CAMEL—Comprehensive areal model of earthquake-induced landslides. *Eng. Geol.* **2009**, *104*, 1–15. [[CrossRef](#)]
5. Wu, W.; Xu, C.; Wang, X.; Tian, Y.; Deng, F. Landslides Triggered by the 3 August 2014 Ludian (China) Mw 6.2 Earthquake: An Updated Inventory and Analysis of Their Spatial Distribution. *J. Earth Sci.* **2020**, *31*, 853–866. [[CrossRef](#)]
6. Budimir, M.E.A.; Atkinson, P.M.; Lewis, H.G. Seismically induced landslide hazard and exposure modelling in Southern California based on the 1994 Northridge, California earthquake event. *Landslides* **2015**, *12*, 895–910. [[CrossRef](#)]
7. Lee, Y.T.; Turcotte, D.L.; Rundle, J.B.; Chen, C.C. Aftershock Statistics of the 1999 Chi-Chi, Taiwan Earthquake and the Concept of Omori Times. *Pure Appl. Geophys.* **2013**, *170*, 221–228. [[CrossRef](#)]
8. Chigira, M.; Wu, X.; Inokuchi, T.; Wang, G. Landslides induced by the 2008 Wenchuan earthquake, Sichuan, China. *Geomorphology* **2010**, *118*, 225–238. [[CrossRef](#)]
9. Cui, P.; Zhang, J.Q.; Yang, Z.J.; Chen, X.Q.; You, Y.; Li, Y. Activity and distribution of geohazards induced by the Lushan earthquake, April 20, 2013. *Nat. Hazards* **2014**, *73*, 711–726. [[CrossRef](#)]
10. Wang, G. Comparison of the landslides triggered by the 2013 Lushan earthquake with those triggered by the strong 2008 Wenchuan earthquake in areas with high seismic intensities. *Bull. Eng. Geol. Environ.* **2015**, *74*, 77–89. [[CrossRef](#)]
11. Xu, C.; Xu, X.; Shyu, J.B.H. Database and spatial distribution of landslides triggered by the Lushan, China Mw 6.6 earthquake of 20 April 2013. *Geomorphology* **2015**, *248*, 77–92. [[CrossRef](#)]
12. Chen, C.-W.; Sato, M.; Yamada, R.; Iida, T.; Matsuda, M.; Chen, H. Modeling of earthquake-induced landslide distributions based on the active fault parameters. *Eng. Geol.* **2022**, *303*, 106640. [[CrossRef](#)]
13. Chang, M.; Cui, P.; Xu, L.; Zhou, Y. The spatial distribution characteristics of coseismic landslides triggered by the Ms7.0 Lushan earthquake and Ms7.0 Jiuzhaigou earthquake in southwest China. *Environ. Sci. Pollut. Res.* **2021**, *28*, 20549–20569. [[CrossRef](#)] [[PubMed](#)]
14. Zhuang, J.; Peng, J.; Xu, C.; Li, Z.; Densmore, A.; Milledge, D.; Iqbal, J.; Cui, Y. Distribution and characteristics of loess landslides triggered by the 1920 Haiyuan Earthquake, Northwest of China. *Geomorphology* **2018**, *314*, 1–12. [[CrossRef](#)]
15. Tian, Y.; Xu, C.; Ma, S.; Xu, X.; Wang, S.; Zhang, H. Inventory and Spatial Distribution of Landslides Triggered by the 8th August 2017 MW 6.5 Jiuzhaigou Earthquake, China. *J. Earth Sci.* **2019**, *30*, 206–217. [[CrossRef](#)]

16. Has, B.; Noro, T.; Maruyama, K.; Nakamura, A.; Ogawa, K.; Onoda, S. Characteristics of earthquake-induced landslides in a heavy snowfall region—Landslides triggered by the northern Nagano prefecture earthquake, March 12, 2011, Japan. *Landslides* **2012**, *9*, 539–546. [[CrossRef](#)]
17. Guo, C.-w.; Huang, Y.-d.; Yao, L.-k.; Alradi, H. Size and spatial distribution of landslides induced by the 2015 Gorkha earthquake in the Bhote Koshi river watershed. *J. Mt. Sci.* **2017**, *14*, 1938–1950. [[CrossRef](#)]
18. Fan, X.; Scaringi, G.; Xu, Q.; Zhan, W.; Dai, L.; Li, Y.; Pei, X.; Yang, Q.; Huang, R. Coseismic landslides triggered by the 8th August 2017 Ms 7.0 Jiuzhaigou earthquake (Sichuan, China): Factors controlling their spatial distribution and implications for the seismogenic blind fault identification. *Landslides* **2018**, *15*, 967–983. [[CrossRef](#)]
19. Chen, X.; Liu, C.; Wang, M. A method for quick assessment of earthquake-triggered landslide hazards: A case study of the Mw6.1 2014 Ludian, China earthquake. *Bull. Eng. Geol. Environ.* **2019**, *78*, 2449–2458. [[CrossRef](#)]
20. Collins, B.D.; Kayen, R.; Tanaka, Y. Spatial distribution of landslides triggered from the 2007 Niigata Chuetsu–Oki Japan Earthquake. *Eng. Geol.* **2012**, *127*, 14–26. [[CrossRef](#)]
21. Meunier, P.; Hovius, N.; Haines, A.J. Regional patterns of earthquake-triggered landslides and their relation to ground motion. *Geophys. Res. Lett.* **2007**, *34*, 1–5. [[CrossRef](#)]
22. Meunier, P.; Hovius, N.; Haines, J.A. Topographic site effects and the location of earthquake induced landslides. *Earth Planet. Sci. Lett.* **2008**, *275*, 221–232. [[CrossRef](#)]
23. Lee, C.-T.; Huang, C.-C.; Lee, J.-F.; Pan, K.-L.; Lin, M.-L.; Dong, J.-J. Statistical approach to earthquake-induced landslide susceptibility. *Eng. Geol.* **2008**, *100*, 43–58. [[CrossRef](#)]
24. Xu, C.; Xu, X. Statistical analysis of landslides caused by the Mw 6.9 Yushu, China, earthquake of April 14, 2010. *Nat. Hazards* **2014**, *72*, 871–893. [[CrossRef](#)]
25. Zhong, X.M.; Xu, X.W.; Chen, W.K.; Liang, Y.X.; Sun, Q.Y. Characteristics of loess landslides triggered by the 1927 Mw8.0 earthquake that occurred in Gulang County, Gansu Province, China. *Front. Environ. Sci.* **2022**, *10*, 1–19. [[CrossRef](#)]
26. Keefer, D.K. Landslides caused by earthquakes. *Geol. Soc. Am. Bull.* **1984**, *95*, 406–421. [[CrossRef](#)]
27. Rodriguez, C.; Bommer, J.; Chandler, R. Earthquake-induced landslides: 1980–1997. *Soil Dyn. Earthq. Eng.* **1999**, *18*, 325–346. [[CrossRef](#)]
28. Keefer, D.K. Statistical analysis of an earthquake-induced landslide distribution—The 1989 Loma Prieta, California event. *Eng. Geol.* **2000**, *58*, 231–249. [[CrossRef](#)]
29. Huang, F.M.; Cao, Z.S.; Jiang, S.H.; Zhou, C.B.; Huang, J.S.; Guo, Z.Z. Landslide susceptibility prediction based on a semi-supervised multiple-layer perceptron model. *Landslides* **2020**, *17*, 2919–2930. [[CrossRef](#)]
30. Su, F.H.; Cui, P.; Zhang, J.Q.; Xiang, L.Z. Susceptibility assessment of landslides caused by the wenchuan earthquake using a logistic regression model. *J. Mt. Sci.* **2010**, *7*, 234–245. [[CrossRef](#)]
31. Zhao, B.; Li, W.L.; Su, L.J.; Wang, Y.S.; Wu, H.C. Insights into the Landslides Triggered by the 2022 Lushan Ms 6.1 Earthquake: Spatial Distribution and Controls. *Remote Sens.* **2022**, *14*, 4365. [[CrossRef](#)]
32. Zhao, B.; Liao, H.J.; Su, L.J. Landslides triggered by the 2018 Lombok earthquake sequence, Indonesia. *Catena* **2021**, *207*, 105676. [[CrossRef](#)]
33. He, X.L.; Xu, C. Spatial distribution and tectonic significance of the landslides triggered by the 2021 Ms6.4 Yangbi earthquake, Yunnan, China. *Front. Earth Sci.* **2022**, *10*, 1–17. [[CrossRef](#)]
34. Dai, F.C.; Xu, C.; Yao, X.; Xu, L.; Tu, X.B.; Gong, Q.M. Spatial distribution of landslides triggered by the 2008 Ms 8.0 Wenchuan earthquake, China. *J. Asian Earth Sci.* **2011**, *40*, 883–895. [[CrossRef](#)]
35. Lu, J.Y.; Li, W.L.; Zhan, W.W.; Tie, Y.B. Distribution and Mobility of Coseismic Landslides Triggered by the 2018 Hokkaido Earthquake in Japan. *Remote Sens.* **2022**, *14*, 3957. [[CrossRef](#)]
36. Zhang, S.; Li, R.; Wang, F.W.; Iio, A. Characteristics of landslides triggered by the 2018 Hokkaido Eastern Iburi earthquake, Northern Japan. *Landslides* **2019**, *16*, 1691–1708. [[CrossRef](#)]
37. Gorum, T.; Fan, X.M.; van Westen, C.J.; Huang, R.Q.; Xu, Q.; Tang, C.; Wang, G.H. Distribution pattern of earthquake-induced landslides triggered by the 12 May 2008 Wenchuan earthquake. *Geomorphology* **2011**, *133*, 152–167. [[CrossRef](#)]
38. Hungr, O.; Leroueil, S.; Picarelli, L. The Varnes classification of landslide types, an update. *Landslides* **2014**, *11*, 167–194. [[CrossRef](#)]
39. Martino, S.; Bozzano, F.; Caporossi, P.; D’angiò, D.; Della Seta, M.; Esposito, C.; Fantini, A.; Fiorucci, M.; Giannini, L.; Iannucci, R. Impact of landslides on transportation routes during the 2016–2017 Central Italy seismic sequence. *Landslides* **2019**, *16*, 1221–1241. [[CrossRef](#)]
40. Shao, X.Y.; Ma, S.Y.; Xu, C. Distribution and characteristics of shallow landslides triggered by the 2018 Mw 7.5 Palu earthquake, Indonesia. *Landslides* **2022**, *20*, 1–19. [[CrossRef](#)]
41. Tang, R.; Fan, X.; Scaringi, G.; Xu, Q.; van Westen, C.J.; Ren, J.; Havenith, H.-B. Distinctive controls on the distribution of river-damming and non-damming landslides induced by the 2008 Wenchuan earthquake. *Bull. Eng. Geol. Environ.* **2019**, *78*, 4075–4093. [[CrossRef](#)]
42. Keefer, D.K. Investigating landslides caused by earthquakes—A historical review. *Surv. Geophys.* **2002**, *23*, 473–510. [[CrossRef](#)]
43. Xu, C.; Xu, X.; Yao, X.; Dai, F. Three (nearly) complete inventories of landslides triggered by the May 12, 2008 Wenchuan Mw 7.9 earthquake of China and their spatial distribution statistical analysis. *Landslides* **2014**, *11*, 441–461. [[CrossRef](#)]
44. Xu, C.; Xu, X.W.; Zhou, B.G.; Yu, G.H. Revisions of the M 8.0 Wenchuan earthquake seismic intensity map based on co-seismic landslide abundance. *Nat. Hazards* **2013**, *69*, 1459–1476. [[CrossRef](#)]

45. Sato, H.P.; Harp, E.L. Interpretation of earthquake-induced landslides triggered by the 12 May 2008, M7.9 Wenchuan earthquake in the Beichuan area, Sichuan Province, China using satellite imagery and Google Earth. *Landslides* **2009**, *6*, 153–159. [[CrossRef](#)]
46. Yin, Y.; Wang, F.; Sun, P. Landslide hazards triggered by the 2008 Wenchuan earthquake, Sichuan, China. *Landslides* **2009**, *6*, 139–152. [[CrossRef](#)]
47. Havenith, H.B.; Vanini, M.; Jongmans, D.; Faccioli, E. Initiation of earthquake-induced slope failure: Influence of topographical and other site specific amplification effects. *J. Seismol.* **2003**, *7*, 397–412. [[CrossRef](#)]
48. Celebi, M. Topographical and geological amplifications determined from strong-motion and aftershock records of the 3 March 1985 Chile earthquake. *Bull. Seismol. Soc. Amer.* **1987**, *77*, 1147–1167. [[CrossRef](#)]
49. Qi, S.; Xu, Q.; Lan, H.; Zhang, B.; Liu, J. Spatial distribution analysis of landslides triggered by 2008.5. 12 Wenchuan Earthquake, China. *Eng. Geol.* **2010**, *116*, 95–108. [[CrossRef](#)]
50. Osmundsen, P.T.; Henderson, I.; Lauknes, T.R.; Larsen, Y.; Redfield, T.F.; Dehls, J. Active normal fault control on landscape and rock-slope failure in northern Norway. *Geology* **2009**, *37*, 135–138. [[CrossRef](#)]
51. Rossi, A.; Tertulliani, A.; Azzaro, R.; Graziani, L.; Rovida, A.; Maramai, A.; Pessina, V.; Hailemichael, S.; Buffarini, G.; Bernardini, F.; et al. The 2016–2017 earthquake sequence in Central Italy: Macroseismic survey and damage scenario through the EMS-98 intensity assessment. *Bull. Earthq. Eng.* **2019**, *17*, 2407–2431. [[CrossRef](#)]
52. Michetti, A.; Esposito, E.; Guerrieri, L.; Porfido, S.; Serva, L.; Tatevossian, R.; Vittori, E.; Audemard, F.; Azuma, T.; Clague, J. Environmental seismic intensity scale-ESI 2007. *Mem. Descr. Carta Geol. D'Ital* **2007**, *74*, 7–23.
53. Serva, L.; Vittori, E.; Comerci, V.; Esposito, E.; Guerrieri, L.; Michetti, A.M.; Mohammadioun, B.; Mohammadioun, G.C.; Porfido, S.; Tatevossian, R.E. Earthquake Hazard and the Environmental Seismic Intensity (ESI) Scale. *Pure Appl. Geophys.* **2016**, *173*, 1479–1515. [[CrossRef](#)]
54. Gosar, A. Application of Environmental Seismic Intensity scale (ESI 2007) to Krn Mountains 1998 M-w=5.6 earthquake (NW Slovenia) with emphasis on rockfalls. *Nat. Hazards Earth Syst. Sci.* **2012**, *12*, 1659–1670. [[CrossRef](#)]
55. Chen, C.W.; Iida, T.; Yamada, R. Effects of active fault types on earthquake-induced deep-seated landslides: A study of historical cases in Japan. *Geomorphology* **2017**, *295*, 680–689. [[CrossRef](#)]
56. Zuccaro, G.; De Gregorio, D.; Titirla, M.; Modano, M.; Rosati, L. On the simulation of the seismic energy transmission mechanisms. *Ing. Sismica* **2018**, *35*, 109–130. [[CrossRef](#)]
57. Sun, D.; Yang, T.; Cao, N.; Qin, L.; Hu, X.; Wei, M.; Meng, M. Characteristics and Prevention of Coseismic Geohazard Induced by Luding Ms 6.8 Earthquake, Sichuan, China. *Earth Sci. Front.* **2022**, *1*, 1–18.
58. Borrelli, L.; Coniglio, S.; Critelli, S.; La Barbera, A.; Gulla, G. Weathering grade in granitoid rocks: The San Giovanni in Fiore area (Calabria, Italy). *J. Maps* **2016**, *12*, 260–275. [[CrossRef](#)]

Disclaimer/Publisher's Note: The statements, opinions and data contained in all publications are solely those of the individual author(s) and contributor(s) and not of MDPI and/or the editor(s). MDPI and/or the editor(s) disclaim responsibility for any injury to people or property resulting from any ideas, methods, instructions or products referred to in the content.